

Phase field modeling of microstructure evolution of electrocatalyst-infiltrated solid oxide fuel cell cathodes

Linyun Liang, Qun Li, Jiamian Hu, Shiwoo Lee, Kirk Gerdes, and Long-Qing Chen

Citation: [Journal of Applied Physics](#) **117**, 065105 (2015); doi: 10.1063/1.4908281

View online: <http://dx.doi.org/10.1063/1.4908281>

View Table of Contents: <http://scitation.aip.org/content/aip/journal/jap/117/6?ver=pdfcov>

Published by the [AIP Publishing](#)

Articles you may be interested in

[Microstructural coarsening effects on redox instability and mechanical damage in solid oxide fuel cell anodes](#)
J. Appl. Phys. **114**, 183519 (2013); 10.1063/1.4830015

[Redox instability, mechanical deformation, and heterogeneous damage accumulation in solid oxide fuel cell anodes](#)

J. Appl. Phys. **112**, 036102 (2012); 10.1063/1.4745038

[Phase-field modeling of three-phase electrode microstructures in solid oxide fuel cells](#)

Appl. Phys. Lett. **101**, 033909 (2012); 10.1063/1.4738230

[Synthesis and calorimetric studies of oxide multilayer systems: Solid oxide fuel cell cathode and electrolyte materials](#)

J. Vac. Sci. Technol. B **28**, C5A1 (2010); 10.1116/1.3420396

[Multielectronic conduction in \$\text{La}_{1-x}\text{Sr}_x\text{Ga}_{1/2}\text{Mn}_{1/2}\text{O}_{3-\delta}\$ as solid oxide fuel cell cathode](#)

J. Appl. Phys. **94**, 1758 (2003); 10.1063/1.1587888



Phase field modeling of microstructure evolution of electrocatalyst-infiltrated solid oxide fuel cell cathodes

Linyun Liang,^{1,a)} Qun Li,¹ Jiamian Hu,¹ Shiwoo Lee,² Kirk Gerdes,² and Long-Qing Chen¹

¹Department of Materials Science and Engineering, The Pennsylvania State University, University Park, Pennsylvania 16802, USA

²National Energy Technology Laboratory, Morgantown, West Virginia 26507, USA

(Received 2 October 2014; accepted 2 February 2015; published online 13 February 2015)

A phase field model is developed to examine microstructural evolution of an infiltrated solid oxide fuel cell cathode. It is employed to generate the three-phase backbone microstructures and morphology of infiltrate nano-particles [La_{1-x}Sr_xMnO₃ (LSM)]. Two-phase Y₂O₃ + ZrO₂ and LSM backbones composed of 0.5–1 μm particles are first generated and then seeded with infiltrate, and evolution is compared for starting infiltrate particle diameters of 5 nm and 10 nm. The computed lifetime triple phase boundary (3PB) density of the infiltrated cathode is then compared to the cathode backbone. Results indicate that initial coarsening of infiltrate nano-particles is the primary evolution process, and infiltrate coarsening is the majority contributor to 3PB reduction. However, at all times, the infiltrated cathode possesses significantly greater 3PB length than even the uncoarsened backbone. Infiltrate particle size effects indicate that the smaller particle size produces greater 3PB length for the same infiltration amount, consistent with intuition. A maximum 3PB enhancement is reached when increasing infiltrate particle loading, and the maximum enhancement depends on infiltrate particle size. It is found that architectural degradation modes will insignificantly affect the lifetime performance of infiltrated cathodes. This work suggests that lifetime optimized particle size/loading combinations are identifiable, and can be precise if additional fundamental data become available. © 2015 AIP Publishing LLC. [<http://dx.doi.org/10.1063/1.4908281>]

I. INTRODUCTION

Solid oxide fuel cells (SOFCs) have been intensively investigated as next-generation energy conversion devices owing to their high fuel-to-electricity conversion efficiency, quiet operation, scalability, and low emission.^{1–4} A conventional cathode is typically a three-phase structure composed of an electronically conductive phase (either La_{1-x}Sr_xMnO₃ (LSM) or La_{1-x}Sr_xCo_{1-y}Fe_yO₃ (LSCF)), an ionically conductive phase (such as Y₂O₃ + ZrO₂ (YSZ)), and a pore phase.^{5,6} The redox reaction occurs at three-phase boundaries (3PBs) where ions and electrons meet with the gas atoms. The cathode performance is directly dependent on the 3PB density and also the transport properties inside the porous electrode microstructures. The porous microstructure feature is to efficiently increase the contact areas of these three phases. Solution infiltration of the inherently functional cathode structure has been reported to improve the performance of SOFCs.^{7–11} Although the introduced infiltrate phase provides more active sites and electronic/ionically conducting paths compared to the backbone microstructures, the long-term morphological stability of the infiltrate is not assured. It is believed that the performance of the infiltrated cathode is closely related to the nano-particle morphology characterized by nano-particle diameter, particle number density, surface area, materials, and particle shape. Variation in such microstructural parameters impacts the infiltrate-backbone

and infiltrate-infiltrate interfacial areas and chemical active sites. The SOFC operating temperature of 750 °C leads to significant surface diffusivities of the infiltrate and backbone particles, which eventually causes the coarsening of global microstructure. Specifically, owing to elevated surface energies and particle sizes, the infiltrated particles may coarsen and agglomerate faster than even the backbone particles themselves, rendering the infiltrate useless.^{12,13} Coarsening theory usually describes the evolution of the nano-particle characteristic length as a time-dependent power law, and the 3PB density decreases during the coarsening processes. In order to correlate the microstructural parameters to the cathode performance, a model of microstructural evolution would engender more rapid evaluation of materials performance over time periods that are experimentally inaccessible.

Given the number of independently adjustable infiltrate fabrication parameters that may have a significant impact to infiltrate efficacy, engineering of a suitable infiltrate phase would be accelerated by the development of a model correlating structure and evolution. As a mesoscopic modeling method, the phase-field approach naturally treats the material interfaces in a diffuse-interface description, which is appropriate to model microstructural morphologies and temporal evolution. There is no need to track the interfaces during the microstructural evolution; therefore, *a priori* assumptions regarding the complex microstructure morphology are not required. Recently, phase field modeling has been applied to model the microstructure degradation both in cathode¹⁴ and anode^{15,16} materials in SOFCs. Typically, the three-phase microstructures are described by a set of conserved phase

^{a)}Author to whom correspondence should be addressed. Electronic mail: lyliang39@gmail.com. Tel: +1 814 865 0389.

composition variables. Within each solid phase, the different orientation grains are represented by the grain order parameters. These phase-field variables have nearly constant values in the bulk materials, which are related to the structure, composition, and orientation of the phases. These variables gradually vary across the narrow interfaces. Their temporal and spatial evolutions are controlled by the Cahn–Hilliard equations for conserved variables and Allen–Cahn equations for order parameters. The reduction of surface energies is the main driving force for the particle coarsening. The evolution of the microstructure is implicitly given by the evolution of the phase-field variables.

In this paper, we extend the phase-field model developed for three-phase cathode microstructures to include an infiltrate phase to study the microstructural evolution of SOFC cathodes modified by the chemical infiltration of nanoparticles. Another phase parameter is introduced to describe the infiltrate phase, and the coarsening of infiltrate particles is governed by the Allen–Cahn kinetics. The main degradation mechanism considered is particle coarsening, although numerous mechanisms exist in reality, including formation of secondary phases and cation inter-diffusion at interfaces.¹⁰ Grain coarsening during cell operation decreases the active area and the 3PB density, and increases the resistance of cathode, which can eventually degrade the cathode performance. The 3PB density initially increases with addition of infiltrate particles, then decreases as particle loading increases. We further report evolution behavior of LSM nanoparticles with different particle sizes infiltrated on LSM/YSZ backbone surfaces. The number of LSM nanoparticles is distributed more on YSZ surfaces than LSM surfaces as shown in our experiments. Microstructural evolution of infiltrate and backbone particles are presented, and the corresponding 3PB density and surface areas are computed with different infiltrate particle sizes and volume fractions.

II. PHASE FIELD MODEL

A porous composite SOFC cathode infiltrated with nanoparticles is generally comprised of four different phases, i.e., electrode- α -phase (electronic conducting), electrolyte- β -phase (ionic conducting), infiltrate- γ -phase (electronic conducting or mixed conducting), and pore- δ -phase (gas conducting), as shown in Fig. 1. The infiltrate particles are assumed to be pure electronic-conducting phase. The infiltrate nanoparticle and backbone LSM phase are belong to the same phase. Therefore, the infiltrate should sit on the backbone surface and connect with the YSZ and pore phases to form a 3PB in order to enhance the performance of cathode. If the infiltrate only contacts with LSM and pore phase or if there is no contact between the infiltrate and YSZ, the 3PB cannot be counted. To describe the phase evolution in such a four-phase system, four composition fields $C_\alpha(r)$, $C_\beta(r)$, $C_\gamma(r)$, and $C_\delta(r)$ are chosen to represent the corresponding phase volume fractions. The composition field variables are defined as $C_\alpha(r) = 1$ for the electrode- α -phase with zero values for all other composition variables, $C_\beta(r) = 1$ for the electrolyte- β -phase, $C_\gamma(r) = 1$ for infiltrate- γ -phase, and $C_\delta(r) = 1$ for pore- δ -phase with same conditions. The

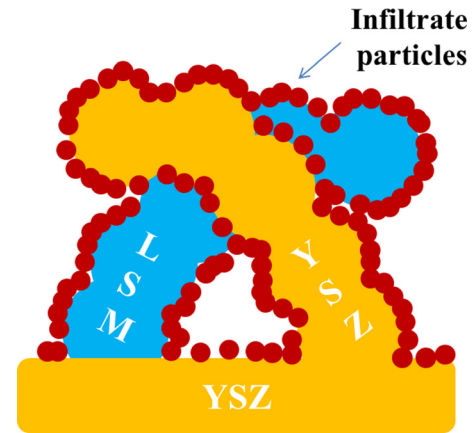


FIG. 1. Schematic description of a three-phase SOFC cathode with infiltration phase system (i.e., electrode- α -phase, electrolyte- β -phase, and infiltrate- γ -phase).

composition variables continuously change across the inter-phase boundary with finite thickness of the diffuse interfaces.¹⁷ The conserved composition fields satisfy the condition $C_\alpha(r) + C_\beta(r) + C_\gamma(r) + C_\delta(r) = 1$. Therefore, three independent field variables C_α , C_β , and C_γ are sufficient to define the conserved compositions of a four-phase system. For three dense solid phases, the crystallographic grain orientations in space can be described by introducing a set of order parameters, $\eta_1^\alpha(r), \eta_2^\alpha(r), \dots, \eta_p^\alpha(r)$ for the α phase, $\eta_1^\beta(r), \eta_2^\beta(r), \dots, \eta_q^\beta(r)$ for the β phase, and $\eta_1^\gamma(r), \eta_2^\gamma(r), \dots, \eta_m^\gamma(r)$ for the γ phase (infiltrate), where p , q , and m are the numbers of possible grain orientations of three solid phases α , β , and γ , respectively. These non-conserved orientation variables change continuously in space and assume continuous values ranging from 0 to 1 across the phase interfaces.

Based on our previous three-phase cathode phase field model, we can write the total free energy as a 4th-order polynomial function in terms of compositions and grain orientation order parameters as^{14,18–20}

$$F = \int \left[f_0(C_\alpha, C_\beta, C_\gamma, \eta_i^\alpha, \eta_j^\beta, \eta_k^\gamma) + \frac{\kappa_C^{\alpha,\beta,\gamma}}{2} (\nabla C_{\alpha,\beta,\gamma})^2 + \sum_{i=1}^{p,q,m} \frac{\kappa_i^{\alpha,\beta,\gamma}}{2} (\nabla \eta_i^{\alpha,\beta,\gamma})^2 \right] dV, \quad (1)$$

where $\nabla C_{\alpha,\beta,\gamma}$ and $\nabla \eta_i^{\alpha,\beta,\gamma}$ are gradients of compositions and order parameters and $\kappa_C^{\alpha,\beta,\gamma}$ and $\kappa_i^{\alpha,\beta,\gamma}$ are their corresponding gradient energy coefficients. The local free energy density f_0 is given by

$$f_0 = f_1(C_\alpha) + f_1(C_\beta) + f_1(C_\gamma) + \sum_{i=1}^p f_2(C_\alpha, \eta_i^\alpha) + \sum_{i=1}^q f_2(C_\beta, \eta_i^\beta) + \sum_{i=1}^m f_2(C_\gamma, \eta_i^\gamma) + \sum_{i=1}^p \sum_{j \neq i}^p f_3(\eta_i^\alpha, \eta_j^\alpha) + \sum_{i=1}^q \sum_{j \neq i}^q f_3(\eta_i^\beta, \eta_j^\beta) + \sum_{i=1}^m \sum_{j \neq i}^m f_3(\eta_i^\gamma, \eta_j^\gamma) + f_4(C_\alpha, C_\beta, C_\gamma), \quad (2)$$

where each energy term can be expressed as

$$\begin{aligned}
f_1(C_{\alpha,\beta,\gamma}) &= -\frac{A}{2}(C_{\alpha,\beta,\gamma} - C_m)^2 + \frac{B}{4}(C_{\alpha,\beta,\gamma} - C_m)^4 \\
&\quad + \frac{D_\alpha}{4}(C_{\alpha,\beta,\gamma} - C_\alpha^0)^4 + \frac{D_\beta}{4}(C_{\alpha,\beta,\gamma} - C_\beta^0)^4 \\
&\quad + \frac{D_\gamma}{4}(C_{\alpha,\beta,\gamma} - C_\gamma^0)^4, \\
f_2(C_{\alpha,\beta,\gamma}, \eta_i^{\alpha,\beta,\gamma}) &= -\frac{\gamma}{2}(C_{\alpha,\beta,\gamma} - C_\alpha^0)^2 (\eta_i^{\alpha,\beta,\gamma})^2 + \frac{\delta}{4} (\eta_i^{\alpha,\beta,\gamma})^4, \\
f_3(\eta_i^{\alpha,\beta,\gamma}, \eta_j^{\alpha,\beta,\gamma}) &= \frac{\varepsilon_{ij}}{2} (\eta_i^{\alpha,\beta,\gamma})^2 (\eta_j^{\alpha,\beta,\gamma})^2, \\
f_4(C_\alpha, C_\beta, C_\gamma) &= \frac{\lambda}{2}(C_\alpha)^2 (C_\beta)^2 + \frac{\lambda}{2}(C_\alpha)^2 (C_\gamma)^2 \\
&\quad + \frac{\lambda}{2}(C_\beta)^2 (C_\gamma)^2. \tag{3}
\end{aligned}$$

Here, $f_1(C_{\alpha,\beta,\gamma})$ is only dependent on the phase composition, $f_2(C_{\alpha,\beta,\gamma}, \eta_i^{\alpha,\beta,\gamma})$ is the function of coupled composition and orientation fields, $f_3(\eta_i^{\alpha,\beta,\gamma}, \eta_j^{\alpha,\beta,\gamma})$ gives the interaction between orientation fields, and $f_4(C_\alpha, C_\beta, C_\gamma)$ represents the interaction between different composition fields.

The spatial and temporal kinetic evolutions of cathode microstructures are controlled by the Allen–Cahn equations and Cahn–Hilliard equations as follows:

For the LSM phase,

$$\begin{aligned}
\frac{\partial \eta_i^\alpha(r, t)}{\partial t} &= -L_i^\alpha \left[\frac{\delta f_0}{\delta \eta_i^\alpha(r, t)} - \kappa_i^\alpha \nabla^2 \eta_i^\alpha \right], \quad i = 1, 2, \dots, p, \\
\frac{\partial C_\alpha(r, t)}{\partial t} &= \nabla M_C^\alpha \nabla \left[\frac{\delta f_0}{\delta C_\alpha(r, t)} - \kappa_C^\alpha \nabla^2 C_\alpha \right], \tag{4}
\end{aligned}$$

for the YSZ phase,

$$\begin{aligned}
\frac{\partial \eta_i^\beta(r, t)}{\partial t} &= -L_i^\beta \left[\frac{\delta f_0}{\delta \eta_i^\beta(r, t)} - \kappa_i^\beta \nabla^2 \eta_i^\beta \right], \quad i = 1, 2, \dots, q, \\
\frac{\partial C_\beta(r, t)}{\partial t} &= \nabla M_C^\beta \nabla \left[\frac{\delta f_0}{\delta C_\beta(r, t)} - \kappa_C^\beta \nabla^2 C_\beta \right], \tag{5}
\end{aligned}$$

and for the infiltrate phase,

$$\begin{aligned}
\frac{\partial \eta_i^\gamma(r, t)}{\partial t} &= -L_i^\gamma \left[\frac{\delta f_0}{\delta \eta_i^\gamma(r, t)} - \kappa_i^\gamma \nabla^2 \eta_i^\gamma \right], \quad i = 1, 2, \dots, m, \\
\frac{\partial C_\gamma(r, t)}{\partial t} &= \nabla M_C^\gamma \nabla \left[\frac{\delta f_0}{\delta C_\gamma(r, t)} - \kappa_C^\gamma \nabla^2 C_\gamma \right], \tag{6}
\end{aligned}$$

where $L_i^{\alpha,\beta,\gamma}$ and $M_C^{\alpha,\beta,\gamma}$ are kinetic coefficients related to grain boundary mobilities and atomic diffusion coefficients, and t is time.

The first procedural step uses Eqs. (4) and (5) to describe backbone evolution for 5000 time steps, which produces LSM and YSZ backbone microstructures with grain sizes consistent with conventionally manufactured SOFC, i.e., 0.5–1 μm . Infiltrate particles are then randomly seeded on the backbone surfaces, and the whole system is permitted to evolve. The expansion coefficients associated with the chemical free energy are ideally informed by the surface

energies of solid phases and interfacial energies between two phases, and the kinetic evolution coefficient should be estimated by the effective diffusion coefficients of solid phases and grain boundary mobilities. Unfortunately, experimental data are not sufficient yet available to confirm all parameter assignments. Therefore, all simulations carried out in this work are based on reasonable dimensionless parameters estimated from literature.¹⁴ The expansion parameters in Eq. (3) are assumed as $C_0 = 0.0$, $C_m = 0.5$, $A = 1.0$, $\varepsilon_{ij} = 3.0$, $\delta = 1.0$, $\lambda = 3.0$, $\gamma = \delta$, $B = 4A$, and $D_\alpha = \gamma^2/\delta$. These chosen parameters ensure that f_0 has degenerate minima with equal depth located at equilibrium states $C_\alpha(r) = 1.0$ and $\eta_i^\alpha = 1.0$ for i -th grain of electrode- α -phase, $C_\beta(r) = 1.0$ and $\eta_j^\beta = 1.0$ for j -th grain of electrolyte- β -phase, $C_\gamma(r) = 1.0$ and $\eta_k^\gamma = 1.0$ for k -th grain of infiltrate- γ -phase, and $C_\delta(r) = 1.0$ and $\eta^\delta = 1.0$ for pore- δ -phase. The other used dimensionless parameters are the gradient coefficients for phase parameters $\kappa_i^\alpha = \kappa_i^\beta = \kappa_i^\gamma = 2.0$, and for volume fraction variables $\kappa_C^\alpha = \kappa_C^\beta = \kappa_C^\gamma = 2.0$ to allow enough grid points at interfaces. The time step for the evolution is $t = 0.3$, and the spacing $dx = dy = dz = 4.0$. The kinetic coefficients for time-dependent Ginzburg–Landau equations are set as $L_i^\alpha = L_i^\beta = 0.004$ and $L_i^\gamma = 0.04$ and mobilities for Cahn–Hilliard equations are $M_C^\alpha = M_C^\beta = 0.008$ and $M_C^\gamma = 0.08$. A model size of $64\Delta x \times 64\Delta y \times 64\Delta z$ is used and periodic boundary conditions are applied along three directions. The semi-implicit Fourier-spectral approximation²¹ is applied to solve Eqs. (4)–(6).

III. RESULTS AND DISCUSSION

Contact angles are first checked at the triple-phase junctions for infiltrate/LSM/pore, infiltrate/YSZ/pore, and LSM/YSZ/pore in two dimensions. Based on the analysis of microstructural morphologies of LSM/YSZ cathode from the Back-scattered Electron images of a porous compact²² and a composite cathode,²³ and neglecting the small differences in surface energies for various surfaces, the contact angles at a triple junction are considered identically 120° in these simulations.²⁴ Figure 2 shows the interfacial configurations of LSM infiltrate particles deposited on the LSM and YSZ backbone surfaces, respectively.

A three-phase LSM/YSZ cathode backbone microstructure is generated from the previously reported phase-field model where three phase volume fractions are prescribed for

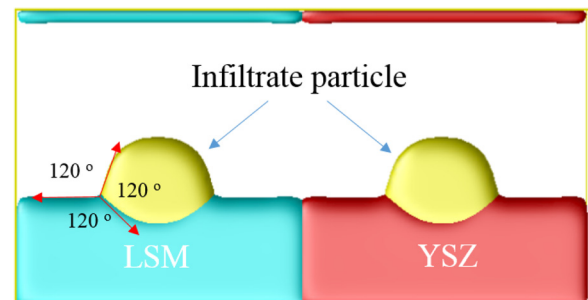


FIG. 2. Interfacial configurations of infiltrate particles sit on the LSM and YSZ phase surface. The ratio of LSM/YSZ interfacial energy (γ_{12}), LSM surface energy (γ_{13}), and YSZ surface energy (γ_{23}) is 1:1:1.

33% electrode- α -phase, 33% electrolyte- β -phase, and 34% pore- γ -phase.¹⁴ Computer 3D simulations are started from a randomly disordered microstructure where the desired volume fraction and the volume conservation are prescribed. Small nuclei of infiltrate phase with particle size around 5 nm are randomly seeded on the LSM and YSZ surfaces once the backbone particle size becomes approximately 1 μm . Based on the experimental observations, the number of nanoparticles distributed on YSZ surfaces is more than on LSM surfaces. It does not necessarily mean that LSM exclusively deposits on YSZ: Infiltrated LSM may form epitaxial nano-scale layer on LSM grains. But it is likely, the volume fraction of LSM infiltrate on YSZ is higher than on LSM. Thus, in our simulations, we also prescribed nearly two times more infiltrate particles on the YSZ surfaces than on the LSM surfaces. Due to the diffuse-interface nature, we can easily tack the YSZ-pore interface and LSM-pore interface based on their composition parameters. Then we randomly add 1000 number of small infiltrate nuclei on the LSM surface and 2000 number of small nuclei on the YSZ surface. The whole system is permitted to evolve by solving governing equations (4)–(6). In Huang's experimental paper, the composite cathode is prepared by infiltration of LSM nanoparticles, of aqueous salt solution, and of molten salts into the porous YSZ. The infiltrate LSM has a high mobility of YSZ surfaces and the final morphology of the infiltrate is independent of the starting particle size and morphology.²⁵ However, we study the different procedure that the LSM infiltrate nanoparticles are randomly seeded into the existing LSM–YSZ composite cathode. In order to study the effects of nano-particle coarsening processes on the evolution, and satisfy the experimental observations, the growth of backbone grains is assumed to be slow.^{12,25,26}

The temporal evolution of cathode microstructure after infiltration is depicted in Fig. 3. The simulated architectural features satisfy the requirements of SOFC cathode design by allowing electronic, ionic, and gas transport through the cathode. Specifically, percolated networks exist that facilitate gas transport through pore-phase (vacuum), oxygen ion transport through electrolyte-phase (red color), and electron transport through electrode- α -phase (green color), with infiltrate particles (yellow color) not percolated.^{27,28} Since the infiltrate particles deposit randomly for most infiltration methods, the backbone surfaces are covered by either dispersed or connected infiltrate nano particles. As shown in Fig. 3, the sizes of LSM and YSZ backbone grains increase slightly during the coarsening processes. The average size of backbone grains is typically 0.5–1.0 μm in diameter, whereas the diameter of infiltrate particles are relatively small, ranging from 10 to 50 nm after 1.3×10^5 time steps. Owing to particle growth over time, the size and number of infiltrate particles increases and decreases, respectively. This particle coarsening process is driven by the reduction of total energy accompanying a minimization of interfacial area.

Recent mathematical models show that properties of cathodes are very sensitive to the infiltrate particle size.^{29–31} To study the infiltrate particle size effects on the microstructure evolutions, we increase the initial diameter of infiltrate particles about two times and seed the same LSM/YSZ

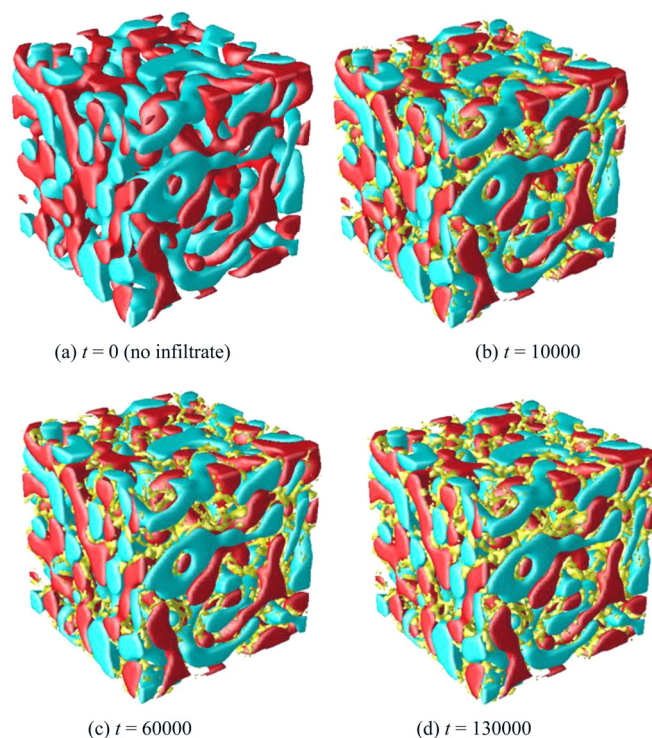


FIG. 3. Temporal evolution of three-phase cathode microstructures infiltrated by nano-particles with sizes around 10–50 nm after 1.3×10^5 time steps. The red, green, and yellow color represents YSZ, LSM, and infiltrate phase, respectively. The vacuum is pore phase.

backbones. The total volume fraction of infiltrate particles is consistent with the first simulation; therefore, the increased particle size results in a diminished absolute number of infiltrate particles compared to the smaller diameter infiltrate. The temporal evolution of infiltrated cathode microstructures is plotted in Fig. 4. The evolved infiltrate grains grow to 50–100 nm after 1.3×10^5 time steps.

Figure 5 compares the time-dependent surface coverage for two infiltrate particle diameters on both LSM and YSZ surfaces. The covered surface area is defined as the ratio of contact areas of infiltrate phase with the backbone surface to the total backbone surface areas. As time goes on, the covered surface areas decreases with the growth of infiltrate nanoparticles. The magnitude of small particle surface coverage is larger than for large particles when the total infiltrate loading is maintained.²⁹ Thus, the lifetime magnitude of surface area covered by infiltrate is largely dependent on the starting particle sizes.

In experiments, grain coarsening decreases both the active area and the 3PB density, and increases the resistance of cathode. According to the definition of 3PBs, they are formed by the contact of percolated LSM and YSZ phases in porous systems, and 3PB length depends on the number of contact points between LSM, YSZ, and pore phases. Infiltrate LSM nano-particles coating the backbone surface can provide a path for electronic conduction. Thus, it is expected that addition of infiltrate directly promotes 3PB density. Figure 6 shows a comparison of 3PB density for non-infiltrated and infiltrated cathode with different initial infiltrate particle sizes. Because electrodes much be electronically conductive, the composite phase needs to be at least

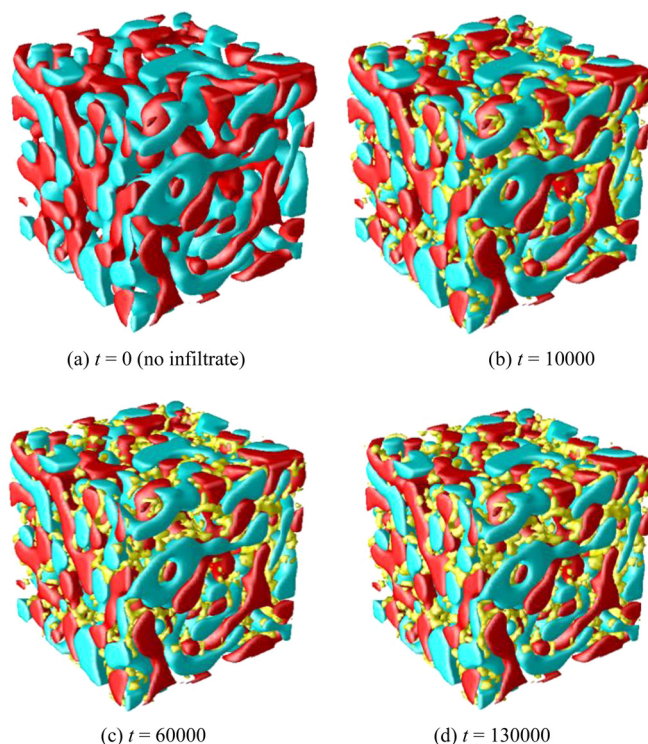


FIG. 4. Temporal evolution of three-phase cathode microstructures infiltrated by nano-particles with sizes around 50–100 nm after 1.3×10^5 time steps. The red, green, and yellow color represents YSZ, LSM, and infiltrate phase, respectively. The vacuum is pore phase.

30% in order for that phase to “percolate” a random structure.³² The backbone LSM and YSZ volume fractions both are set as 33%. The measurement of 3PB length is identified as the edges where three different voxels, each of which belongs to a different phase, are in contact. The infiltrate LSM and backbone LSM are taken as the same phase. The 3PB density is defined as the 3PB length divided by the cell volume. The total 3PB density can be divided into two parts, the backbone particles with pore phase as well as the infiltrate particle with YSZ and pore phase. Here, we assume that all 3PBs are active. It is clearly seen that the values of 3PB

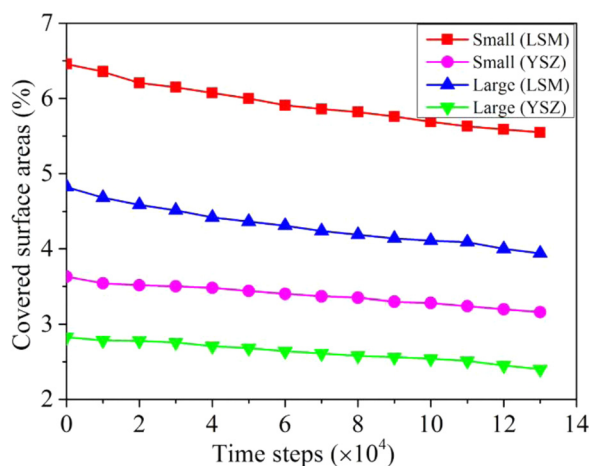


FIG. 5. Different initial infiltrate particle size effects on the infiltrate covered areas for the LSM and YSZ surfaces, respectively. The diameters of small and large infiltrate particles are 10–50 nm and 50–100 nm after 1.3×10^5 time steps, respectively.

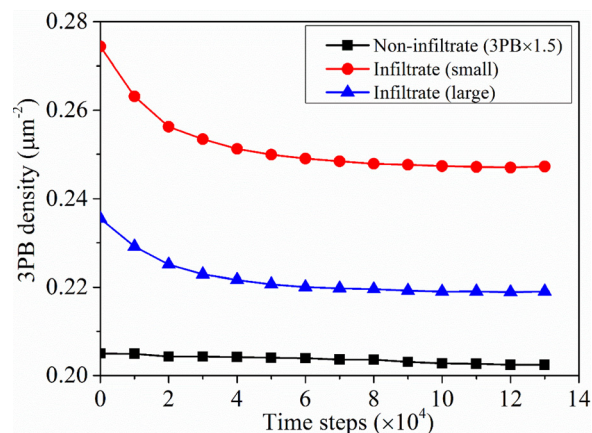


FIG. 6. Comparison of the calculated 3PB density of backbone and infiltrated cathode as a function of time steps. The values of 3PB density for non-infiltrated cathode is multiplied by 1.5.

density for the infiltrated cathode with different infiltrate particle sizes largely increase, which is consistent with the results predicted by experiments and mathematical model.³³ Generally, the isolated infiltrate nanoparticle close to the backbone 3PB resulting in a further increase of the 3PB is beneficial for the electrochemical performance. The improvement in 3PB not only provides more effective pathway for electrons in the electrode but also more reaction sites for the reduction reaction. Plenty of experimental results concluded that the infiltration can significantly increase the electronic conductivity and reduce the overpotential of the cathode.^{7,11,34–37} The lifetime 3PB density evolution shows that infiltrate coarsening mainly occurs at the initial stage, which agrees with the experimental observation of resistances where the main performance changes occur at the initial stage.^{12,38,39} For example, Shah *et al.*¹² studied the coarsening of LSCF nanoparticle affect the polarization resistance. The degradation is more rapid in the early stages. The high aging temperature (800 °C) can cause the nanoparticle size increase from 40 nm to 120 nm after 300 h. As expected, the decreasing 3PB density mainly arises from the coarsening of infiltrate particles but not from the backbone microstructure, which is consistent with the microstructure evolution in Figs. 3 and 4. The cathode with small infiltrate particle gives larger 3PB density than the larger infiltrate particle over the lifetime, which suggests that the small and uniform particle size can produce a better cathode performance.^{29–31} The coarsening of infiltrate particles as a function of time is also consistent with the evolution of surface coverage, as shown in Fig. 5. In all cases tested here, the infiltrated cathode is expected to retain high 3PB length throughout the operational lifetime, and exhibits superior lifetime 3PB density than the as-fabricated cathode backbone.

3PB density is examined for various infiltrate particle volume fractions using smaller particle size (10–50 nm), and results are depicted in Fig. 7. 3PB density increases with increasing infiltrate loading to a maximum volume fraction at 1.6%. Continued increases in infiltrate loading causes the 3PB fraction to decrease, and significant 3PB density depression is shown for a volume fraction $>2.2\%$. This can be easily understood by considering the relationship between

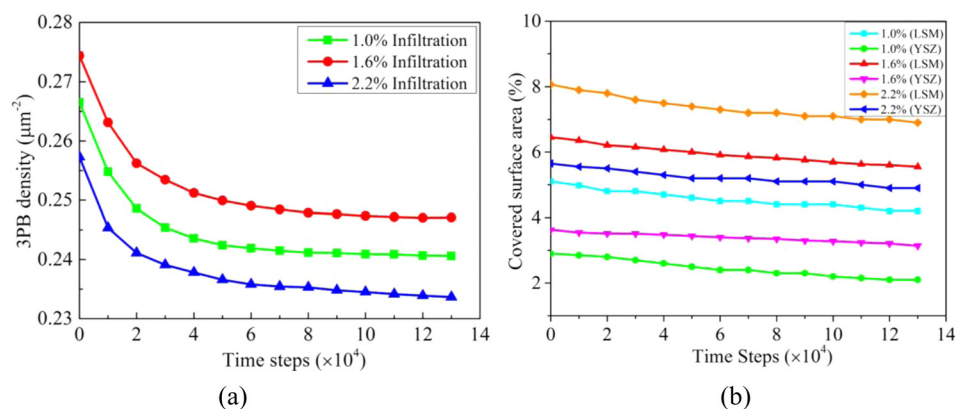


FIG. 7. Different amount of infiltrate particles effects on the (a) 3PB density and their corresponding (b) covered surface area as a function of time steps of an infiltrated LSM/YSZ cathode.

perimeter and interfacial area of the approximately hemispherical particles being applied to the surface. Such a result has been confirmed experimentally. Liang *et al.*⁴⁰ showed that a range of infiltrate particle loading on the backbone surfaces can produce a maximum in cathode performance. The measurement of polarization resistance at different Pd loading demonstrated that the cathode with 5 wt. % Pd loading has the highest value, while it has lower values both for 0.5 wt. % and 25 wt. % loading because of the reduced 3PB for electrochemical reaction. Liu *et al.*⁴¹ recently reported the different $\text{La}_{0.4875}\text{Ca}_{0.0125}\text{Ce}_{0.5}\text{O}_{2-\delta}$ LCC concentration infiltrate the mixed ionic-electronic porous conductor LSCF. The measurement of interfacial polarization resistance has the lowest value at the intermediate LCC concentration 0.25 mol l^{-1} , while both lower and higher LCC concentrations like 0.05 mol l^{-1} and 0.50 mol l^{-1} gave higher resistances. Recent mathematical models also indicated that the peak of 3PB can be obtained by a certain infiltration loading.^{29,31} Therefore, our simulation results also support experimental and computational evidence of optimal infiltrate particle loading for high cathode performance for a particular particle size.

IV. CONCLUSIONS

A phase field model is developed to simulate SOFC microstructures and corresponding evolution of infiltrated cathodes. The enhancement of cathode performance is confirmed by the calculations of 3PBs, which increase largely after the infiltration treatment compared with the non-infiltrated cathode. The time evolution of 3PBs shows that the most rapid evolution occurs at the initial stage. The measurement of infiltrate covered surface area and 3PB density by adding different sizes of initial LSM nanoparticles indicate that the cathode performance largely depends on infiltrate particle sizes. The smaller infiltrate particles give better cathode performance for a certain amount of infiltration solution. At all times, the infiltrated cathode possesses significantly greater 3PB length than even the uncoarsened backbone, and architectural degradation modes will insignificantly affect the lifetime performance of infiltrated cathodes. For a specific particle size, there exists an optimized infiltrate particle loading for the highest cathode performance. Quantitative analysis of the infiltrated cathode associated with microstructural evolution requires thermodynamic and

kinetic parameters from experiments or first-principle calculations such as surface diffusivities of solid phases, grain boundary mobilities, and grain boundary energies. Beyond the electronic conducting infiltrate particles coating on the LSM/YSZ backbone surfaces, our methodology is also valid for the ionic conducting phase coating on the backbone surfaces.

ACKNOWLEDGMENTS

We would like to thank the financial support the National Energy Technology Laboratory's on-going research in the area of cathode modeling in Solid Oxide Fuel Cells under the URS Contract No. 0004000.3.621.054.001.211.000.007.

- ¹A. J. Jacobson, *Chem. Mater.* **22**(3), 660–674 (2010).
- ²C. W. Sun, R. Hui, and J. Roller, *J. Solid State Electrochem.* **14**(7), 1125–1144 (2010).
- ³E. V. Tsipis and V. V. Kharton, *J. Solid State Electrochem.* **12**(11), 1367–1391 (2008).
- ⁴N. Q. Minh, *J. Am. Ceram. Soc.* **76**(3), 563–588 (1993).
- ⁵S. P. Jiang, *J. Mater. Sci.* **43**(21), 6799–6833 (2008).
- ⁶J. Richter, P. Holtappels, T. Graule, T. Nakamura, and L. J. Gauckler, *Monatsh. Chem.* **140**(9), 985–999 (2009).
- ⁷J. M. Vohs and R. J. Gorte, *Adv. Mater.* **21**(9), 943–956 (2009).
- ⁸S. P. Jiang, *Int. J. Hydrogen Energy* **37**(1), 449–470 (2012).
- ⁹C. Lu, T. Z. Sholklapper, C. P. Jacobson, S. J. Visco, and L. C. De Jonghe, *J. Electrochem. Soc.* **153**(6), A1115–A1119 (2006).
- ¹⁰S. Lee, N. Miller, H. Abernathy, K. Gerdes, and A. Manivannan, *J. Electrochem. Soc.* **158**(6), B735–B742 (2011).
- ¹¹Z. Y. Jiang, C. R. Xia, and F. L. Chen, *Electrochim. Acta* **55**(11), 3595–3605 (2010).
- ¹²M. Shah, P. W. Voorhees, and S. A. Barnett, *Solid State Ionics* **187**(1), 64–67 (2011).
- ¹³M. Shah, G. A. Hughes, P. W. Voorhees, and S. A. Barnett, in *Solid Oxide Fuel Cells 12*, edited by S. C. Singhal and K. Eguchi (ECS Transactions, 2011), Vol. 35, pp. 2045–2053.
- ¹⁴Q. Li, L. Y. Liang, K. Gerdes, and L. Q. Chen, *Appl. Phys. Lett.* **101**(3), 033909 (2012).
- ¹⁵H. Y. Chen, H. C. Yu, J. S. Cronin, J. R. Wilson, S. A. Barnett, and K. Thornton, *J. Power Sources* **196**(3), 1333–1337 (2011).
- ¹⁶J. H. Kim, W. K. Liu, and C. Lee, *Comput. Mech.* **44**(5), 683–703 (2009).
- ¹⁷L. Q. Chen, *Annu. Rev. Mater. Res.* **32**, 113–140 (2002).
- ¹⁸D. N. Fan, S. P. Chen, L. Q. Chen, and P. W. Voorhees, *Acta Mater.* **50**(8), 1895–1907 (2002).
- ¹⁹L. Y. Liang, M. Stan, and M. Anitescu, *Appl. Phys. Lett.* **105**(16), 163903 (2014).
- ²⁰L. Y. Liang, Y. Qi, F. Xue, S. Bhattacharya, S. J. Harris, and L. Q. Chen, *Phys. Rev. E* **86**(5), 051609 (2012).
- ²¹L. Q. Chen and J. Shen, *Comput. Phys. Commun.* **108**(2–3), 147–158 (1998).
- ²²A. K. Sahu, A. Ghosh, A. K. Suri, P. Sengupta, and K. Bhanumurthy, *Mater. Lett.* **58**(26), 3332–3336 (2004).
- ²³S. J. Dillon, L. Helmick, H. M. Miller, L. Wilson, R. Gemman, R. V. Petrova, K. Barmak, G. S. Rohrer, and P. A. Salvador, *J. Am. Ceram. Soc.* **94**(11), 4045–4051 (2011).

- ²⁴Y. Zhang, C. Xia, and M. Ni, *Int. J. Hydrogen Energy* **37**(4), 3392–3402 (2012).
- ²⁵Y. Huang, J. M. Vohs, and R. J. Gorte, *Electrochem. Solid State Lett.* **9**(5), A237–A240 (2006).
- ²⁶W. S. Wang, M. D. Gross, J. M. Vohs, and R. J. Gorte, *J. Electrochem. Soc.* **154**(5), B439–B445 (2007).
- ²⁷Y. Ji, K. Yuan, and J. N. Chung, *J. Power Sources* **165**(2), 774–785 (2007).
- ²⁸T. Z. Sholkapper, H. Kurokawa, C. P. Jacobson, S. J. Visco, and L. C. De Jonghe, *Nano Lett.* **7**(7), 2136–2141 (2007).
- ²⁹Y. X. Zhang, Q. Sun, C. R. Xia, and M. Ni, *J. Electrochem. Soc.* **160**(3), F278–F289 (2013).
- ³⁰A. Bertei, J. G. Pharoah, D. A. W. Gowel, and C. Nicolella, *J. Electrochem. Soc.* **161**(12), F1243–F1253 (2014).
- ³¹A. J. L. Reszka, R. C. Snyder, and M. D. Gross, *J. Electrochem. Soc.* **161**(12), F1176–F1183 (2014).
- ³²D. W. Dees, T. D. Claar, T. E. Easler, D. C. Fee, and F. C. Mrazek, *J. Electrochem. Soc.* **134**(9), 2141–2146 (1987).
- ³³W. Zhu, D. Ding, and C. Xia, *Electrochem. Solid State Lett.* **11**(6), B83–B86 (2008).
- ³⁴R. Kiebach, C. Knofel, F. Bozza, T. Klemenso, and C. Chatzichristodoulou, *J. Power Sources* **228**, 170–177 (2013).
- ³⁵X. Y. Lou, S. Z. Wang, Z. Liu, L. Yang, and M. L. Liu, *Solid State Ionics* **180**(23–25), 1285–1289 (2009).
- ³⁶Y. K. Lee, J. Y. Kim, Y. K. Lee, I. Kim, H. S. Moon, J. W. Park, C. P. Jacobson, and S. J. Visco, *J. Power Sources* **115**(2), 219–228 (2003).
- ³⁷T. Z. Sholkapper, C. P. Jacobson, S. J. Visco, and L. C. De Jonghe, *Fuel Cells* **8**(5), 303–312 (2008).
- ³⁸A. Buyukaksoy, V. Petrovsky, and F. Dogan, *J. Electrochem. Soc.* **159**(6), B666–B669 (2012).
- ³⁹A. Samson, M. Sogaard, R. Knibbe, and N. Bonanos, *J. Electrochem. Soc.* **158**(6), B650–B659 (2011).
- ⁴⁰F. L. Liang, W. Zhou, B. Chi, J. Pu, S. P. Jiang, and L. Jian, *Int. J. Hydrogen Energy* **36**(13), 7670–7676 (2011).
- ⁴¹M. F. Liu, D. Ding, K. Blinn, X. X. Li, L. F. Nie, and M. Liu, *Int. J. Hydrogen Energy* **37**(10), 8613–8620 (2012).